Research Square

Preprints are preliminary reports that have not undergone peer review. They should not be considered conclusive, used to inform clinical practice, or referenced by the media as validated information.

High-Fidelity Spatial Photonic Ising Machines via Precise Wavefront Shaping

Pavlos Savvidis

p.savvidis@westlake.edu.cn

Westlake University https://orcid.org/0000-0002-8186-6679

Dimitris Karanikolopoulos

Westlake University

Panagiotis Karavelas

University of Crete and Foundation for Research and Technology-Hellas

Leonidas Mouchliadis

University of Crete and Foundation for Research and Technology-Hellas https://orcid.org/0000-0002-6290-4158

Alexandros Spiliotis

Westlake University https://orcid.org/0000-0003-4051-4439

Nikolaos Pitanios

University of Crete and Foundation for Research and Technology-Hellas

Silvia Gentilini

Sapienza University of Rome

Daniele Veraldi

Sapienza University of Rome

Paolo Charlesworth

Sapienza University of Rome

Davide Pierangeli

Sapienza University of Rome

Jason Sakellariou

QUBITECH

Natalia Berloff

University of Cambridge

Simeon Tsintzos

QUBITECH

Claudio Conti

Sapienza University of Rome https://orcid.org/0000-0003-2583-3415

Article

Keywords:

Posted Date: May 19th, 2026

DOI: https://doi.org/10.21203/rs.3.rs-8740905/v1

License: This work is licensed under a Creative Commons Attribution 4.0 International License.
Read Full License

Additional Declarations: There is no conflict of interest

High-Fidelity Spatial Photonic Ising Machines via Precise Wavefront Shaping

D. Karanikolopoulos[1], P.S. Karavelas*[1,2,3], L. Mouchliadis[2,4], A. K. Spiliotis[1], N. L. Pitanios[1,2,4], S. Gentilini[6,8], D. Veraldi[6], P. Charlesworth[6], D. Pierangeli[6], J. Sakellariou[5], N. G. Berloff[7], S. I. Tsintzos[5], C. Conti[6] and P. G. Savvidis*[1,2,4]

1. Department of Physics, School of Science, Westlake University, Hangzhou 310014, China
2. Center for Quantum Science & Technologies, FORTH-QuTech, Heraklion 70013, Crete, Greece
3. Department of Physics, University of Crete, Heraklion 70013, Crete, Greece
4. Department of Materials Science and Engineering, University of Crete, Heraklion 70013, Crete, Greece
5. QUBITECH Thessalias 8, GR 15231 Chalandri, Athens, Greece
6. Department of Physics, Sapienza University, Piazzale Aldo Moro 5, 00185 Rome, Italy
7. Department of Applied Mathematics and Theoretical Physics, University of Cambridge, Cambridge CB3 0WA, United Kingdom
8. Institute for Complex Systems, National Research Council (ISC-CNR), Via dei Taurini 19, 00185 Rome, Italy

* corresponding authors

Abstract

Ising machines are emerging as a powerful physical alternative to digital processors for solving combinatorial optimization problems. Among them, spatial photonic Ising machines (SPIMs) offer compact, room-temperature hardware with inherently parallel, energy efficient, single-shot optical evaluation of the Ising Hamiltonian. However, scalability has been fundamentally limited by optical aberrations and non-uniform illumination, which corrupt phase-based spin encoding and distort coupling representation, forcing operation to a restricted spatial light modulator (SLM) region. Here we introduce a high-precision full-aperture calibration scheme that overcomes these constraints. By implementing wavefront retrieval and correction with $< \lambda/40$ accuracy, we restore faithful phase encoding across the entire SLM area. Furthermore, we introduce a novel interaction-normalization method, which compensates for amplitude curvature and enables uniform coupling representation. Together, these advances establish a high-fidelity, full-area SPIM architecture that unlocks true scalability and enables larger and more reliable photonic Ising computations.

Introduction

The Ising model is a cornerstone of statistical mechanics and a powerful framework for solving combinatorial optimization problems by mapping them to the search for low-energy configurations of an Ising Hamiltonian[1–3]. Many NP-hard problems can be formulated as Quadratic Unconstrained Binary Optimization (QUBO) tasks, turning combinatorial search into an energy-minimization problem well suited for physics-inspired hardware acceleration[2]. Ising machines exploit this principle by allowing a physical system to evolve toward low-energy states, providing candidate solutions to optimization problems[3]. This capability has led to wide interest across applications including scheduling[4], materials science[5], protein folding[6], chemical design[7], finance[8], traffic[9], communication[10].

Among existing approaches, photonic Ising machines[5,11–18] are particularly promising because they implement spins and interactions using optical fields, enabling massive parallelism and low latency. Optical propagation can perform global summations or inner products in a single step, offering the potential for high throughput and improved energy efficiency compared with electronic systems[19–22]. In this context, spatial photonic Ising machines encode spins in the spatial degrees of freedom of a coherent optical field and use propagation and detection to evaluate Hamiltonian terms in parallel. Typically, spins are implemented by assigning each lattice site to a spatial region of a spatial light modulator that applies discrete phase values (commonly 0 or π). After the SLM, a lens performs a Fourier transform so that the far-field intensity measured by a camera becomes a quadratic function of the output field, computing weighted sums of pairwise spin products through interference. This enables single-shot optical evaluation of the Ising energy with high resolution and large dynamic range, making SPIMs attractive for NP-hard tasks such as max-cut, spin-glass ground-state search, graph partitioning, and other QUBO formulations.

A central challenge, however, is the encoding of arbitrary dense coupling matrices J, which are not addressed by the initial SPIM approach [12], restricted only to Mattis type Ising Hamiltonians[23]. Implementing general interactions therefore requires decomposition strategies—such as eigen decomposition or low-rank approximations—followed by space-, wavelength-, or time-division multiplexing[24–29]. Another approach was to use an extra ancilla spin that will help select the integrating information on the focal plane, allowing for arbitrary interaction encoding[30].

Importantly, SPIM performance is strongly limited by wavefront distortion and amplitude non-uniformity, both of which compromise accurate Hamiltonian encoding. Aberrations arise inevitably from imperfect optical elements and distort the propagated wavefront, leading to incorrect phase mappings and errors in effective spin interactions. Similarly, a uniform amplitude profile is required for precise interaction encoding [12]. For this reason, many SPIM implementations restrict operation to a central SLM region where aberrations are minimized[12,25,31–36]. However, enlarging the usable area amplifies distortion effects and restricts scalability. Even small wavefront deviations can cause incorrect mapping, preventing reliable use of the full SLM aperture.

A recent hybrid photonic–electronic platform significantly advanced SPIM scalability by introducing aberration correction and a dynamic-cluster-flipping algorithm[37]. Expanding upon this framework, our method implements comprehensive, simultaneous correction of both phase and intensity. This approach overcomes previous spatial constraints, enabling accurate interaction encoding across the entire SLM aperture and maximizing the usable computational density. Notably, our phase correction operates without an external interferometer, eliminating sensitivity to thermal or vibrational drifts and the need for active stabilization. We implement a high-precision wavefront retrieval method that enables compensation of optical aberrations with root mean square error $<\lambda/40$ level[38,39]. Furthermore, we address a secondary critical challenge: beam expansion typically introduces a non-uniform Gaussian intensity profile, which acts as a spatially dependent weight and degrades coupling accuracy. We resolve this by normalizing the encoded interactions using the retrieved amplitude profile, thereby ensuring uniform coupling and enabling full utilization of the SLM surface.

Results

The comprehensive wavefront correction scheme is detailed in Figure 1, illustrating the retrieval procedure adapted from Schroff *et al.*[39]. This common-path approach extracts the local phase difference across the SLM plane by interfering a fixed reference region with a scanning sampled region, producing the self-referenced interferograms shown in Fig. 1a. This method allows for high-precision mapping of phase deviations without the need for an external reference beam. The phase values, $\delta\varphi$, which are extracted by fitting the interferograms between a sampled region and the reference are used to construct a corrective phase mask, that compensates for optical distortions (Figure 1c), effectively restoring a flat laser phase front (Figure 1f). This correction achieves high precision, with a root-mean-square accuracy of λ/40

and a peak-to-valley deviation of approximately λ/6. Implementing this correction ensures that each phase-encoded spin state represents the intended Ising model configuration.

The performance of the SPIM critically depends on its ability to detect single spin-flip events and accurately quantify their contribution to the total Ising energy, which is measured as the optical intensity on the focal plane[24,25]. The influence of a single spin flip on the recorded Ising energy can be evaluated, by first measuring the intensity when all spins are uniformly polarized in one direction, and then measuring the intensity after flipping a selected spin. The corresponding diffraction patterns on the camera are shown in the inset of Fig. 1b. By subtracting the intensity in the single-flip configuration from the fully polarized intensity, the individual contribution of the flipped spin to the Ising energy of the Mattis model $H(\sigma) = \sum_{i,j} \xi_i \xi_j \sigma_i \sigma_j$ ferromagnetic interaction $\xi_i = \xi > 0$, is expected to approximately match the optical field intensity at the position of the flipped spin. By systematically scanning the entire spin lattice, this method allows for the experimental retrieval of each spin's contribution to the Ising energy and effectively reconstructs the optical field intensity distribution across the SLM (Figures 1d, g, j).

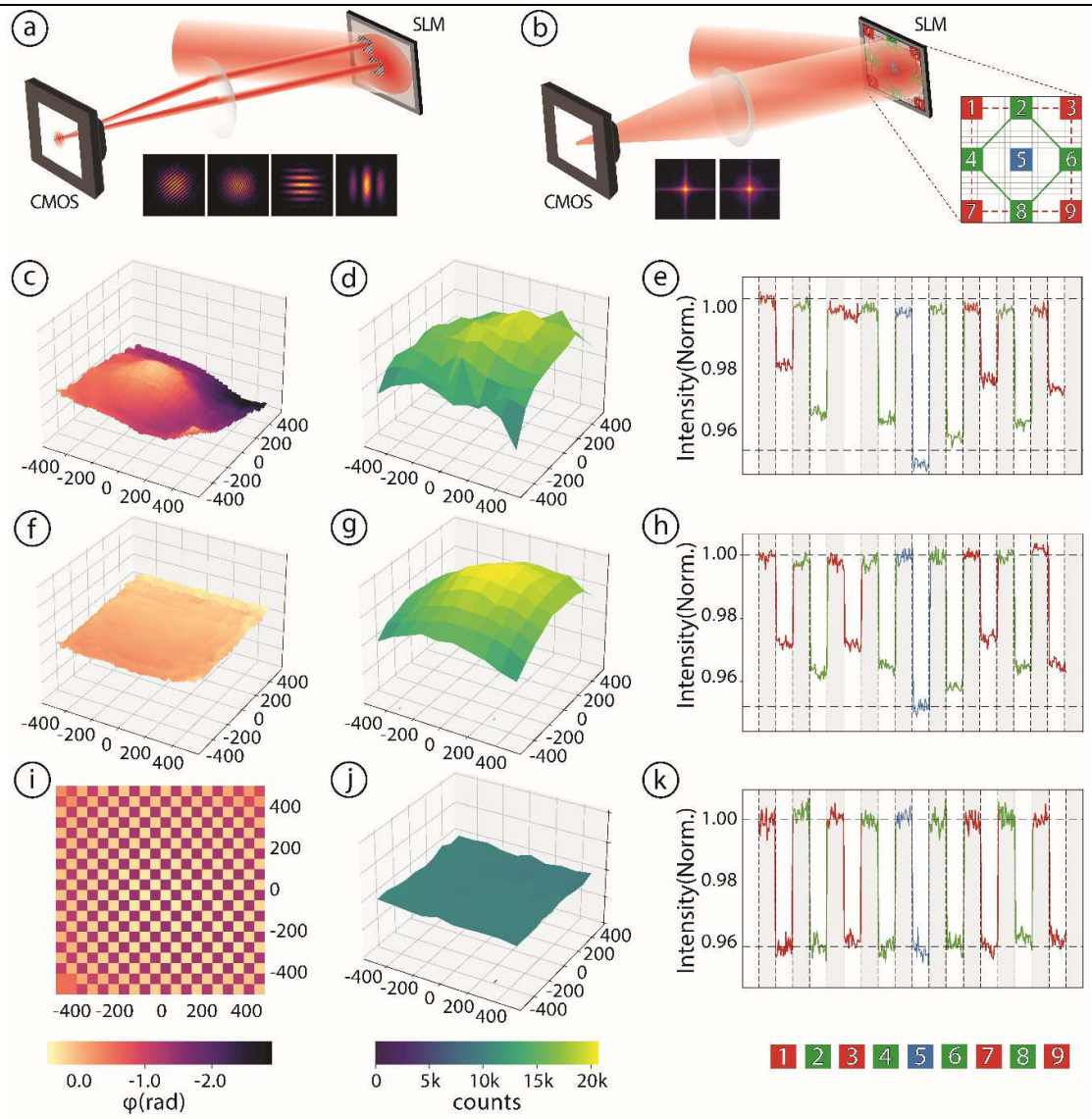

Figure 1. **Wavefront retrieval and correction Methods***:* Schematics of (a) the phase retrieval method, where the inset shows four representative interferograms, and (b) the field intensity retrieval process where the inset shows the diffraction patterns that correspond to the fully polarized and the not fully polarized spin configurations. *Phase correction*: (c) Retrieved phase variation before and (f) after phase correction. *Intensity correction*: (d) Reconstructed optical field intensity distribution across the SLM, before any correction application, (g) after applying phase correction and (j) after applying both phase correction and amplitude flattening. (i) The checkerboard pattern on the SLM, implementing the amplitude flattening. *Spin flip diagnostic test*: (e) before corrections, (h) after only phase correction and (k) with both phase correction and amplitude flattening.

Prior to the use of the correction mask Fig. 1c, the reconstructed intensity does not follow the anticipated Gaussian distribution, but rather a distorted profile (Fig. 1d). The impact of this distorted wavefront is further illustrated in Fig. 1e through a diagnostic spin-flip experiment. In this test, a subset of nine representative spins, schematically indicated in Fig. 1b as differently colored SLM pixels, are sequentially flipped. For each spin-flip event, the corresponding contribution to the overall intensity is measured. The results reveal that the distorted wavefront introduces a local phase offset at the spin encoding sites, leading to spins which are either nonresponsive (Fig. 1e) or do not contribute in accordance with the encoded interaction coupling. Importantly, this effect scales with the physical SLM size, presenting a fundamental limitation to the scalability of SPIMs.

We proceed to calibrate the SPIM implementation by first applying the calculated correction mask on the SLM to compensate for the optical aberrations. This results in the desired flat phase profile illustrated in Fig. 1f. and to an intensity distribution shown in Fig. 1g where the Gaussian profile is restored. In addition, a fundamental prerequisite for reliably mapping spin system problems onto SPIMs is the accurate implementation of inter-spin interactions. To enable full-area utilization of the SLM, we analyze the measured intensity profile in Fig. 1g and observe pronounced non-uniformity across the illuminated region. Conceptually, the inherent Gaussian beam profile (Fig. 1g) can be understood as introducing an additional, unintended layer of interactions embedded within the beam itself. Building on the work of Fang *et al.*[32,33,40] who demonstrated that both spin configurations and inter-spin interactions can be encoded using a single SLM, improving upon earlier approaches requiring two separate SLMs [12,31,34,41,42] we aim to compensate the non-uniform Gaussian intensity profile using a phase-only SLM. Guided by this encoding principle, we design a suitable transformation that ensures the resulting amplitude after interference matches the minimum amplitude of the initial field (see SM for more details). This transformation can be generalized as an interaction normalization method, that removes the additional interaction layer, caused by the non-uniformity of the optical beam. As demonstrated in Figure 1j, the encoding scheme produces the expected uniform intensity profile for ferromagnetic (FM) interactions ($\xi_i = \xi > 0$), where all spins contribute equally. The improvement is further verified by spin-flip diagnostics: while the previous implementation showed variations in spin-flip contributions as large as 45% (Figure 1h), the optimized system reduces this discrepancy to less than 10% (Figure 1k).

The calibration of the SPIM is completed with this final step, ensuring accurate and precise encoding of Ising spins and their interactions. This initialization is crucial for implementing

photonic simulations as expected from the theoretical Ising model Hamiltonian at the full SLM area.

In recent study, Sakellariou *et al.*[30] proposed a calibration approach that correlates experimentally measured with theoretically predicted energies. This approach involves computing the energy of different spin configurations using both the SPIM and the analytical Sherrington-Kirkpatrick (SK) model hamiltonian[43]. A linear regression is then used to correlate the results from these two methods. For the SPIM to accurately simulate the encoded problem, a linear relation between the two energy sets is expected. This is consistent with existing literature, provided that the wavefront (both phase and amplitude) is relatively flat, to ensure accurate problem encoding.

Our results show that achieving such uniformity across the entire SLM region, is an essential initial step. Phase correction enables the calibration of the system's capacity for spin configuration representation, while interaction normalization ensures precise encoding of spin couplings. To demonstrate the effect of these corrections on the relationship between the two energies, we conducted both numerical simulations and experimental measurements. To evaluate the influence of the normalized encoding, we solved a Mattis spin glass model with interaction couplings $\xi_i = \pm 1$.

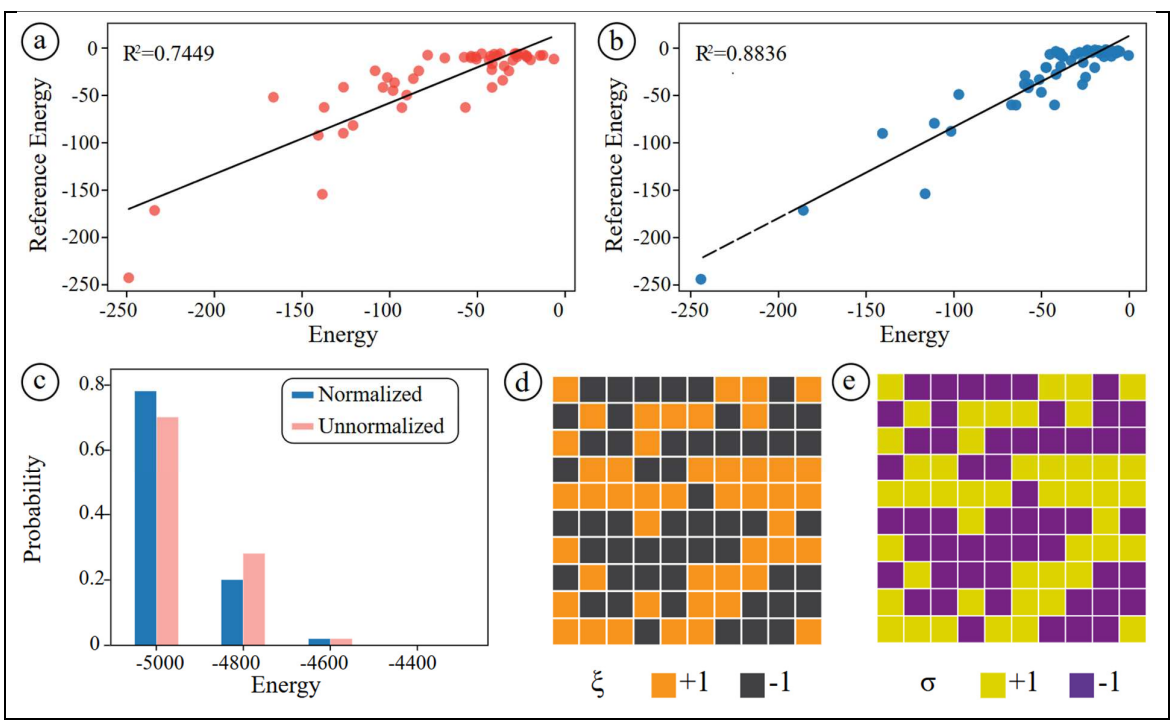

Figure 2. **Comparison of Normalized vs Un-normalized Interactions**. (a-b) Correlation between experimental intensities and the analytical Mattis Hamiltonian *before* (a) and *after* (b)interaction normalization (c) Comparison of ground state search experiments between the two cases of normalized and un-normalized interactions over 50 experiments of 1000 Metropolis-Hastings steps at T=0. (d) Interaction coupling for the Mattis spin glass problem (e) Calculated ground state of the system, consistent with the vector ξ_i.

The selection of this model is based on its simplicity in evaluating ground-state energies. In Mattis-type interaction systems, the expected ground-state spin configuration coincides with the vector ξ_i[1,12] or its inverse, and can therefore be directly verified (Figure 2d,e). The objective of this study is to assess the system's ability to accurately encode interactions, based on both energy calibration and convergence towards the ground state. As illustrated in Figure 2a, the correlation between the analytical Mattis Hamiltonian and the experimentally retrieved energies using unnormalized interactions demonstrates a substantial mismatch. As demonstrated in Figure 2b, the application of interaction normalization resulted in enhanced agreement, thereby improving the system's Hamiltonian representation. Subsequent to the calibration procedure, the experiment was repeated 50 times using the Metropolis–Hastings algorithm with 1000 steps at T=0. The normalization process has been shown to significantly improve the performance of the ground-state search (see Figure 2c). For the normalized case, we observe an improved fidelity with $R^2 = 0.88$. When interactions are improperly normalized and in the absence of compensation the Ising machine is significantly affected by experimental artifacts.

Sampled Spin Lattices – Paving the way to full scalability

We proceed to show that precise wavefront correction is a key enabler of SPIM scalability, allowing accurate encoding over the full SLM aperture. To achieve this, we conduct two distinct experimental procedures. The first approach tests FM interactions by gradually increasing the system size and observing the effects on configuration, energy, magnetization, and stability. However, as the system size increases, this method proves extremely time-consuming, prompting the design of an alternative experiment with the same constraints but greater efficiency. This modified experiment utilizes sampled macropixels distributed across the entire SLM region, as shown in Figure 3a. By covering the full SLM surface, phase

distortion and amplitude curvature effects can be tracked by focusing only on a subset of representative spins. The scalability test is conducted by keeping a constant working area on the SLM (960 × 960 pixels) while decreasing the macropixel size. This method enables the experimental realization of progressively larger spin lattices, aiming to determine the minimum macropixel size required to solve the ferromagnetic interaction problem. We test macropixels with side lengths of 48, 32, 24, 15, and 10 pixels, which correspond to mimicking lattices of 400, 900, 1600, 4096, and 9216 spins, respectively. Note that in these spin lattice simulations, we employ a subset of 100 spins equally distributed across the SLM region while we do not use the rest of the SLM area. This sparse sampling approach ensures coverage of the entire active SLM area while maintaining computational efficiency, hence we use the term *sampled spin lattices*.

Following each experimental convergence event, we perform three post-processing steps: (i) domain standardization:

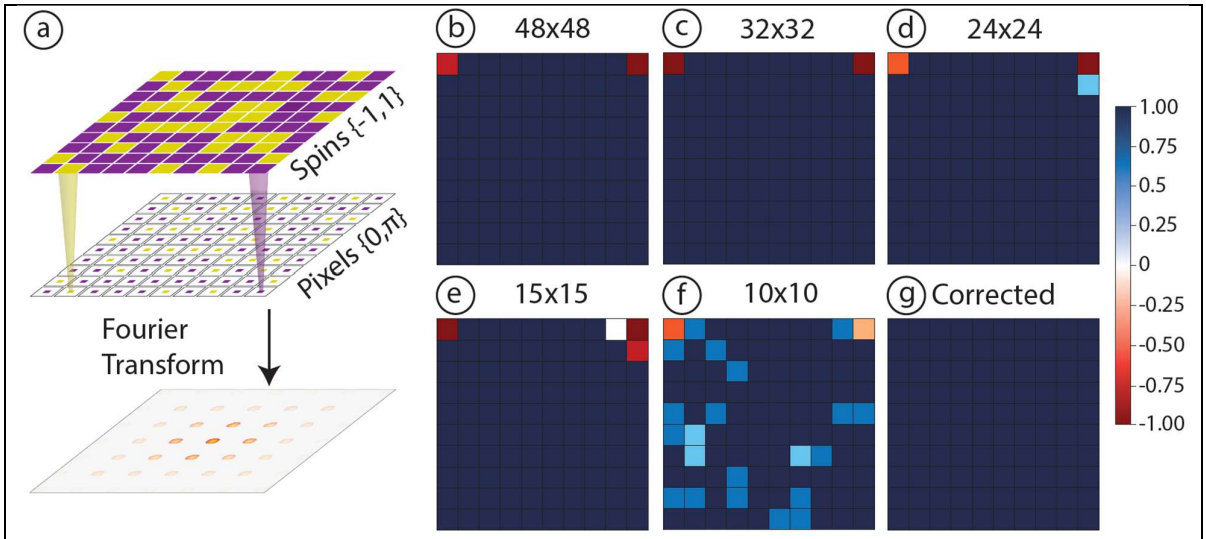

Figure 3. Experimental demonstration of sampled spin lattices, including mean spin configurations. (a) Schematic of the experimental procedure for generating sampled spin lattices (b)-(f) Mean spin configurations from ten FM ground state search runs *without* phase correction, for five different MP sizes, after the three post processing steps. (g) Mean spin configurations from ten FM ground state search runs *with* phase correction for all MP sizes.

we manually normalize the resulting spin configuration by setting the largest domain equal to $+1$ and all remaining spins (or smaller domains) equal to -1 (ii) ensemble averaging: we repeat this process across 10 independent convergence trials (iii*)* statistical analysis: the final mean spin configuration is computed as the ensemble average of all standardized configurations. This post-processing ensures consistent comparison across trials while preserving the dominant domain structure in our statistical analysis.

In Figs. 3b-3f, we show the average spin polarization in the final state configuration for five different macropixel (MP) sizes, before applying the SPIM calibration (phase correction and amplitude normalization). Without SPIM calibration, the final state deviates from the fully polarized FM ground state for all MP sizes. This deviation becomes more pronounced as the MP size decreases and correspondingly the spin lattice size increases, suggesting that while the Metropolis algorithm drives the system toward its ground state, some spins—particularly at the edges of the SLM, where optical aberrations are strongest—fail to align with the dominant orientation. In contrast, after correcting for optical aberrations, the system converges to the theoretically expected FM ground state, with all spins uniformly polarized, regardless of MP size (Fig. 3g). This confirms that SPIM calibration ensures a faithful representation of the Ising Hamiltonian. Notably, for the smallest MP size tested (10 × 10 pixels), this approach combined with averaging could enable spin lattices of up to ~10,000 spins, demonstrating a clear path towards fully scalable SPIMs.

To further support the effect of the SPIM calibration, we focus on the magnetization as the key observable, tracking its convergence towards the FM ground state, which corresponds to a fully polarized spin system with a magnetization value of unity. In Fig. 4a we present the magnetization for three different lattice sizes of 100, 400, and 900 spins using the full lattice approach. Upon convergence to the FM ground state the system exhibits magnetization deviating from unity, with this deviation becoming increasinly larger as the system size increases. The latter indicates that although the Metropolis algorithm converges, the final state spin configuration does not correspond to that of a FM ground state with all spins polarized. In contrast, when the phase correction mask is applied the magnetization converges to unity for all three lattices as expected from the theoretical FM ground state solution of the Ising model (Fig. 4b). Similarly, Figs. 4c and 4d display the magnetization before and after phase correction, respectively, for the sampled spin lattice method. In the uncorrected case, the final-state magnetization fails converge to unity as the macropixel size decreases. However, with

phase correction, the system achieves complete spin polarization even for the largest spin lattices examined.

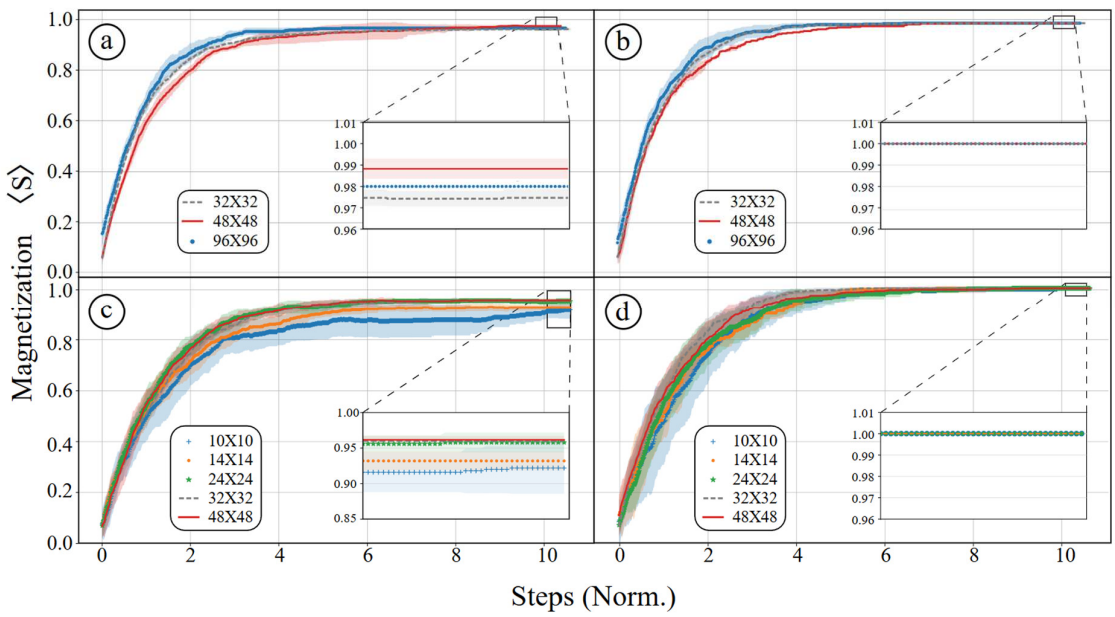

Figure 4. **Effect of phase correction on magnetization with increasing lattice size, using two experimental procedures.** (a) Magnetization for three lattice sizes—100, 400, and 900 spins—before phase correction. (b) Magnetization for the same lattice sizes after applying phase correction. In both cases, convergence steps are normalized by the number of spins. In (c) and (d), we similarly track the magnetization before and after phase correction, respectively, this time by reducing the macropixel lattice mask size while keeping the same ROI and spin lattice size, mimicking spin lattices with sizes ranging from 400 to 9,216 spins.

Discussion

The performance of spatial photonic Ising machines critically depends on accurate mapping between the Ising model spin values and interactions and the phases encoded on the SLM. Aberrations, which arise from imperfections in optical components or misalignments,

introduce deviations in the phase profile, leading to errors in the representation of spin states and coupling interactions. These errors manifest as a mismatch between the physical system and the mathematical model, reducing the accuracy of the solution. Compensating for aberrations is therefore crucial as it directly impacts on the fidelity of the Ising model representation on the SLM. As demonstrated by our analysis, a phase retrieval and consequent phase correction along with amplitude normalization to ensure constant phase and intensity across the entire SLM area is not merely a means to increase its performance in terms of speed and computational accuracy but rather a *sine qua non* procedure for correctly implementing the Ising Hamiltonian on a SPIM. Especially when the issue of scalability is considered, the phase and amplitude calibration proposed in this study renders itself as an indispensable initialization step of next generation SPIMs.

Our methodology bridges the gap between theoretical Ising models and physical implementations of SPIM. By demonstrating that optical imperfections can be systematically corrected, we resolve a key limitation that has hindered the reliable application of SPIMs to large-scale problems. This opens the way for further advancements in scalable SPIMs. Compact photonic Ising machines[25,30] may adopt our techniques to enhance portability without sacrificing accuracy.

While our approach achieves remarkable precision, several challenges remain to achieve fully scalable SPIMs. For instance, thermally induced wavefront drift or SLM aging may necessitate adaptive, real-time correction algorithms designed to address dynamic aberrations. Additionally, enhancing energy measurement efficiency could improve the ability of the system to deduct if a spin flip shall be accepted or not.

In conclusion, by rigorously addressing phase and amplitude non-idealities, we have demonstrated a pathway to fully scalable SPIMs. Our results confirm that optical Ising machines can faithfully emulate spin systems when physical encodings are precisely controlled, a prerequisite for their adoption in real-world optimization tasks. Future work should explore these techniques in non-ideal environments and for non-uniform interaction topologies.

Materials and Methods

SPIM Setup

Our base laser system is a CW laser (Toptica ibeam Smart) with a central wavelength of λ=811 nm. The beam is initially coupled to a single mode fiber, which serves as a spatial filter that creates a clean Gaussian wavefront. At the fiber exit, the beam is collimated by an f = 36 mm fiber collimator, and set to horizontal polarization by a polarizing beam splitter. A combination of f_1 = -50 mm and f_2 = 400 mm lenses is used to expand the beam, before we direct it to the SLM (Hamamatsu x13138). This ensures that the full SLM screen is covered. With the use of a blazed grating phase on the SLM, the beam is then directed to lens L3 (f3=300 mm), where it gets focused on the CMOS camera (Hamamatsu Orca qCMOS) for detection.

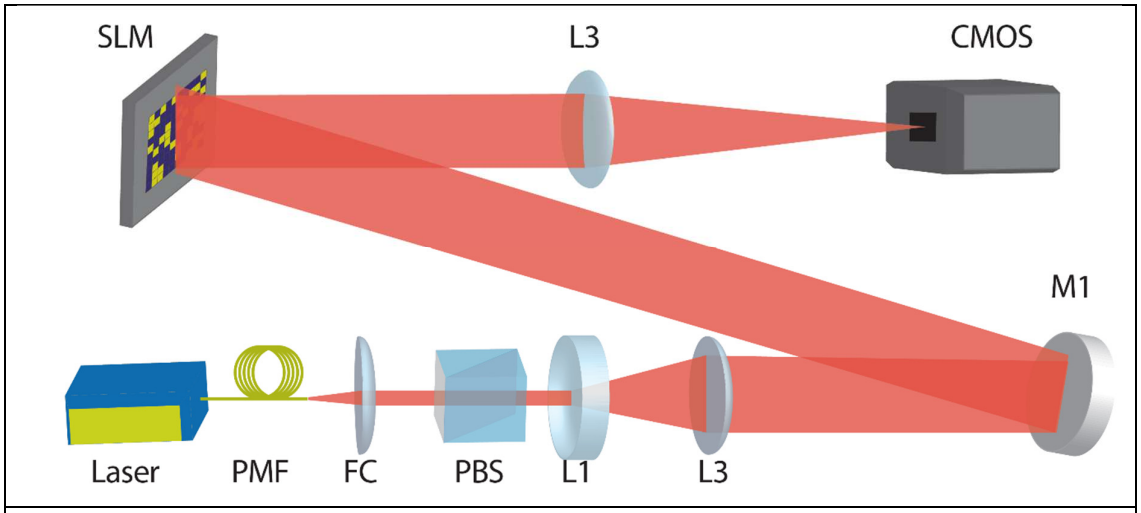

Figure 5: Schematic of the experimental setup

Phase Retrieval Method

A reference and a sample grating aperture phase mask on the SLM produces an interferogram on the image plane which is then recorded by the camera. Inset: Four representative

interferograms illustrating variations based on the relative distance and angle between the sample and reference apertures, corresponding to masks covering different regions on the SLM.

Intensity Retrieval Method

After applying the calculated correction phase on the SLM, we generate a spin configuration corresponding to the ground state of a ferromagnetic Ising model.

To determine the individual contributions of each spin, we systematically flip each spin one at a time and measure the resulting change in the system's response. By aggregating these individual contributions, we reconstruct the intensity profile of the optical beam.

Sampled Spins

A spin-size-specific mask is applied to the SLM spin configuration, defining the lattice geometry. By maintaining the positions of the spins on the SLM while decreasing their MP size, we generate the corresponding masks for each spin lattice.After Fourier transformation via the lens, distinct diffraction spots emerge on the image plane. As the macropixel size decreases, the spatial distribution of these spots changes, leading to corresponding changes in the recorded image on the camera.

Data availability

The data that support the findings of this study are available from the corresponding author upon reasonable request.

Acknowledgements

A. K. S. and P. G. S. acknowledge the support of innovation Program for Quantum Science and technology (2023Zd0300300), and Zhejiang Provincial natural Science Foundation (Xhd24A2401). Financial support from the Horizon EIC- 2022 Pathfinderchallenges-01 HEISINGBERG project 101114978 is acknowledged. This work was supported by the European Union NextGenerationEU through Greece 2.0 National Recovery and Resilience Plan, under the Call SUB.1.1 Clusters of Research Excellence (CREs), under Project QuInPhoS ΥΠ3ΤΑ-0561193.

Conflict of Interest

All authors declare that they have no conflict of interest.

References

1. Nishimori, H. *Statistical Physics of Spin Glasses and Information Processing: An Introduction*. (Oxford University PressOxford, 2001). doi:10.1093/acprof:oso/9780198509417.001.0001.
2. Lucas, A. Ising formulations of many NP problems. *Front. Phys.* **2**, (2014).
3. Zhang, T. *et al.* A Review of Ising Machines Implemented in Conventional and Emerging Technologies. *IEEE Trans. Nanotechnol.* **23**, 704–717 (2024).
4. Venturelli, D., Marchand, D. J. J. & Rojo, G. Quantum Annealing Implementation of Job-Shop Scheduling. Preprint at https://doi.org/10.48550/arXiv.1506.08479 (2016).
5. Gao, Y. *et al.* Photonic Ising machines for combinatorial optimization problems. *Appl. Phys. Rev.* **11**, 041307 (2024).
6. Perdomo-Ortiz, A., Dickson, N., Drew-Brook, M., Rose, G. & Aspuru-Guzik, A. Finding low-energy conformations of lattice protein models by quantum annealing. *Sci. Rep.* **2**, 571 (2012).
7. Mao, Z., Matsuda, Y., Tamura, R. & Tsuda, K. Chemical design with GPU-based Ising machines. *Digit. Discov.* **2**, 1098–1103 (2023).
8. Sornette, D. Physics and financial economics (1776–2014): puzzles, Ising and agent-based models. *Rep. Prog. Phys.* **77**, 062001 (2014).
9. Hu, Z. *et al.* Programmable optoelectronic Ising machine for optimization of real-world problems. *Light Sci. Appl.* **15**, 6 (2026).
10. Otsuka, T. *et al.* High-Speed Resource Allocation Algorithm Using a Coherent Ising Machine for NOMA Systems. *IEEE Trans. Veh. Technol.* **73**, 707–723 (2024).

11. Roques-Carmes, C. *et al.* Heuristic recurrent algorithms for photonic Ising machines. *Nat. Commun.* **11**, 249 (2020).
12. Pierangeli, D., Marcucci, G. & Conti, C. Large-Scale Photonic Ising Machine by Spatial Light Modulation. *Phys. Rev. Lett.* **122**, 213902 (2019).
13. Calvanese Strinati, M., Pierangeli, D. & Conti, C. All-Optical Scalable Spatial Coherent Ising Machine. *Phys. Rev. Appl.* **16**, 054022 (2021).
14. Honjo, T. *et al.* 100,000-spin coherent Ising machine. *Sci. Adv.* **7**, eabh0952 (2021).
15. McMahon, P. L. *et al.* A fully programmable 100-spin coherent Ising machine with all-to-all connections. *Science* **354**, 614–617 (2016).
16. Inagaki, T. *et al.* A coherent Ising machine for 2000-node optimization problems. *Science* **354**, 603–606 (2016).
17. Prabhakar, A. *et al.* Optimization with photonic wave-based annealers. *Philos. Trans. R. Soc. Math. Phys. Eng. Sci.* **381**, 20210409 (2023).
18. Fabre, C. The optical Ising machine. *Nat. Photonics* **8**, 883–884 (2014).
19. Minzioni, P. *et al.* Roadmap on all-optical processing. *J. Opt.* **21**, 063001 (2019).
20. McMahon, P. L. The physics of optical computing. *Nat. Rev. Phys.* **5**, 717–734 (2023).
21. Kari, S. R. *et al.* Optical and Electrical Memories for Analog Optical Computing. *IEEE J. Sel. Top. Quantum Electron.* **29**, 1–12 (2023).
22. Kibebe, C. G., Liu, Y. & Tang, J. Harnessing optical advantages in computing: a review of current and future trends. *Front. Phys.* **12**, 1379051 (2024).
23. Mattis, D. C. Solvable spin systems with random interactions. *Phys. Lett. A* **56**, 421–422 (1976).
24. Wang, S., Zhang, W., Ye, X. & He, Z. General spatial photonic Ising machine based on the interaction matrix eigendecomposition method. *Appl. Opt.* **63**, 2973 (2024).

25. Veraldi, D. *et al.* Fully Programmable Spatial Photonic Ising Machine by Focal Plane Division. *Phys. Rev. Lett.* **134**, 063802 (2025).
26. Sakabe, T. *et al.* Spatial-photonic Ising machine by space-division multiplexing with physically tunable coefficients of a multi-component model. *Opt. Express* **31**, 44127 (2023).
27. Ouyang, J. *et al.* On-demand photonic Ising machine with simplified Hamiltonian calculation by phase encoding and intensity detection. *Commun. Phys.* **7**, 168 (2024).
28. Wang, R. Z. *et al.* Efficient computation using spatial-photonic Ising machines with low-rank and circulant matrix constraints. *Commun. Phys.* **8**, 86 (2025).
29. Luo, L., Mi, Z., Huang, J. & Ruan, Z. Wavelength-division multiplexing optical Ising simulator enabling fully programmable spin couplings and external magnetic fields. *Sci. Adv.* **9**, eadg6238 (2023).
30. Sakellariou, J., Askitopoulos, A., Pastras, G. & Tsintzos, S. I. Encoding Arbitrary Ising Hamiltonians on Spatial Photonic Ising Machines. *Phys. Rev. Lett.* **134**, 203801 (2025).
31. Pierangeli, D., Marcucci, G., Brunner, D. & Conti, C. Noise-enhanced spatial-photonic Ising machine. *Nanophotonics* **9**, 4109–4116 (2020).
32. Fang, Y., Huang, J. & Ruan, Z. Experimental Observation of Phase Transitions in Spatial Photonic Ising Machine. *Phys. Rev. Lett.* **127**, 043902 (2021).
33. Huang, J., Fang, Y. & Ruan, Z. Antiferromagnetic spatial photonic Ising machine through optoelectronic correlation computing. *Commun. Phys.* **4**, 242 (2021).
34. Pierangeli, D., Marcucci, G. & Conti, C. Adiabatic evolution on a spatial-photonic Ising machine. *Optica* **7**, 1535 (2020).
35. Ramesh, V., Natarajan, V. & Prabhakar, A. Solving the two-way Number-Partitioning Problem using a Spatial-Photonic Ising Machine. in *2021 IEEE Photonics Society*

Summer Topicals Meeting Series (SUM) 1–2 (IEEE, Cabo San Lucas, Mexico, 2021). doi:10.1109/SUM48717.2021.9505909.

36. Sun, W., Zhang, W., Liu, Y., Liu, Q. & He, Z. Quadrature photonic spatial Ising machine. *Opt. Lett.* **47**, 1498 (2022).
37. Yao, J., Zhu, R. & Yu, J. Enhanced, fully connected 360 000-spin spatial photonic Ising machine. *Phys. Rev. Appl.* **24**, 044087 (2025).
38. Zupancic, P. *et al.* Ultra-precise holographic beam shaping for microscopic quantum control. *Opt. Express* **24**, 13881 (2016).
39. Schroff, P., La Rooij, A., Haller, E. & Kuhr, S. Accurate holographic light potentials using pixel crosstalk modelling. *Sci. Rep.* **13**, 3252 (2023).
40. Mendoza-Yero, O., Mínguez-Vega, G. & Lancis, J. Encoding complex fields by using a phase-only optical element. *Opt. Lett.* **39**, 1740 (2014).
41. Yamashita, H. *et al.* Low-Rank Combinatorial Optimization and Statistical Learning by Spatial Photonic Ising Machine. *Phys. Rev. Lett.* **131**, 063801 (2023).
42. Shimomura, S., Ogura, Y. & Tanida, J. Parallel processing of spatial photonic Ising machines using spatial multiplexing. in *Machine Learning in Photonics* (eds Ferranti, F., Hedayati, M. K. & Fratalocchi, A.) 79 (SPIE, Strasbourg, France, 2024). doi:10.1117/12.3028713.
43. Sherrington, D. & Kirkpatrick, S. Solvable Model of a Spin-Glass. *Phys. Rev. Lett.* **35**, 1792–1796 (1975).

Author Contributions

P. S. K., D. K., A. K. S. and P.G.S. designed the experiment. D. K. and P. S. K. performed the experiments and analyzed the data. D. K., P. S. K., and J. S. developed the software for data acquisition. P. S. K., and L.M. developed the theory and carried out numerical simulations. N.

L. P. and provided technical support. P.G.S. supervised the project. All authors contributed to the preparation of the manuscript.

Supplementary Files

This is a list of supplementary files associated with this preprint. Click to download.

- LightScienceApplicationsSupFINAL.pdf